Delft University of Technology

Compact Metasurface Terahertz Spectrometer

Ji, Wenye; Chang, Jin; Mirzaei, Behnam; Ridder, Marcel; Jellema, Willem; Kao, Tsung Yu; Lee, Alan; Gao, Jian Rong; Urbach, Hendrik Paul; Adam, Aurèle J.L.

Citation (APA)
Ji, W., Chang, J., Mirzaei, B., Ridder, M., Jellema, W., Kao, T. Y., Lee, A., Gao, J. R., Urbach, H. P., & Adam, A. J. L. (2024). Compact Metasurface Terahertz Spectrometer. *Laser and Photonics Reviews*, *19*(3), Article 2401290. https://doi.org/10.1002/lpor.202401290

Important note
To cite this publication, please use the final published version (if applicable).
Please check the document version above.

Compact Metasurface Terahertz Spectrometer

Wenye Ji,* Jin Chang, Behnam Mirzaei, Marcel Ridder, Willem Jellema, Tsung-Yu Kao, Alan Lee, Jian Rong Gao, Hendrik Paul Urbach, and Aurèle J. L. Adam

The terahertz frequency region of the electromagnetic spectrum is crucial for understanding the formation and evolution of galaxies and stars throughout the universe's history, as well as the process of planet formation. Detecting the unique spectral signatures of molecules and atoms requires terahertz spectrometers, which must be operated in space observatories due to water vapor absorption in the Earth's atmosphere. However, current terahertz spectrometers face challenges such as low resolution, limited bandwidth, large volume, and complexity. In this paper, the issues of size and weight are addressed by demonstrating a concept for a centimeter-sized, low-weight terahertz spectrometer using a metasurface. The design of the metasurface spectrometer is first discussed for the 1.85 to 2.4 THz range, followed by its fabrication. Next, an array of quantum cascade lasers operating at slightly different frequencies around 2.1 THz is utilized to characterize the spectrometer. Finally, a spectrum inversion method is applied to analyze the measured data, confirming a resolution R ($\lambda/\Delta\lambda$) of at least 273. This concept can be extended to other application areas, such as planetary observations and various wavelengths in the far-infrared (FIR) and near-infrared (NIR) ranges.

W. Ji, B. Mirzaei, J. R. Gao, H. P. Urbach, A. J. L. Adam
Department of Imaging Physics
Delft University of Technology
Lorentzweg 1, Delft 2628 CJ, The Netherlands
E-mail: W.Ji@tudelft.nl
J. Chang
Department of Quantum Nanoscience
Delft University of Technology
Lorentzweg 1, Delft 2628 CJ, The Netherlands
M. Ridder, W. Jellema, J. R. Gao
SRON Netherlands Institute for Space Research
Niels Bohrweg 4, 2333 CA Leiden and Landleven 12, Groningen 9747 AD,
The Netherlands
T.-Y. Kao, A. Lee
LongWave Photonics LLC
Mountain View, CA 94043, USA

1. Introduction

Spectroscopic observations play an important role for space astronomy in the terahertz (THz) frequencies or at far-infrared (FIR) wavelengths, where the radiation can provide answers to some key questions on the formation and evolution of galaxies and stars throughout the history of the universe and the process of planet formation. It is known that the temperatures and densities within the star-forming clouds excite the constituent atoms and molecules to produce emission and absorption lines, many of which occur at THz frequencies. Furthermore, the long wavelength nature of THz radiation allows for a study of the active interiors of galaxies throughout cosmic history because galaxies are inherently dusty, causing dust to absorb the short, visible wavelength light and re-radiates the energy in the FIR.[1]

A spectrometer forms the heart of many astronomical instruments at THz.[1] Typically, one applies grating spectrometers or Fourier transform spectrometers (FTS) as low and medium resolution spectrometers, with a spectral resolution (R) of 10^2–10^4, while heterodyne receivers as high-resolution spectrometers can reach an R of higher than 10^6. The R is defined as the average wavelength divided by the wavelength interval which can be resolved by a spectrometer. The choice of a spectrometer depends on the type of observations and the scientific goals.[2] The Herschel Space Observatory, launched in 2009 by the ESA, had all three types of spectrometers on board, covering the wavelength span between 60 and 700 µm.[3] The observatory must be operated from space because the Earth's atmosphere is opaque over most of the FIR wavelengths.

Grating spectrometers are interesting because of their sensitivity, resolution, bandwidth and imaging capability when they are combined with a large, low noise detector array of more than 10^3 pixels. They are highly sought after to study distant galaxies with extremely faint signals, where an R of 10^2–10^4 is sufficient.[4–6] A few space mission concepts, such as SAFARI-SPICA,[4] the Origins Space Telescope (OST),[5] and Galaxy Evolution Probe (GEP),[6] have proposed to use grating spectrometers. In contrast to FTS, grating spectrometers acquire spectral data by diffracting light through a grating without the involvement of movable components, making them mechanically uncomplicated. A
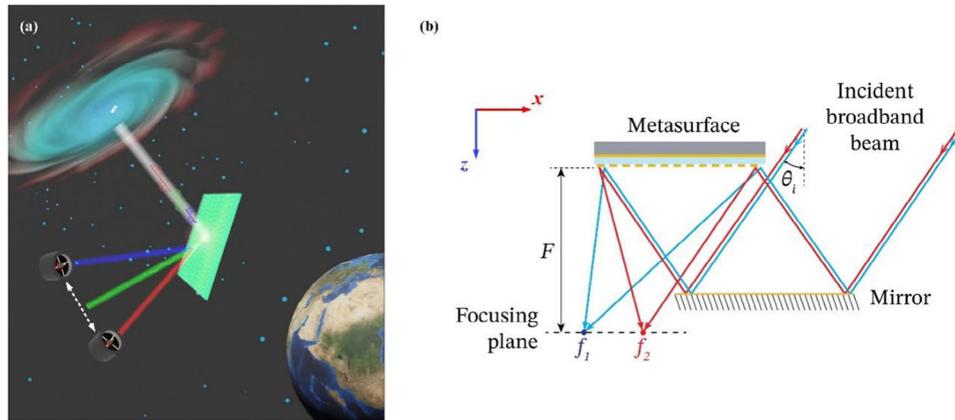
Figure 1. Schematic of a compact metasurface terahertz spectrometer. a) The THz wave in space is incident on the spectrometer. The lights of different wavelengths, they are deflected and focused on different positions in the focusing plane. b) The detailed schematic of our terahertz metasurface spectrometer concept.

typical THz grating spectrometer consists of a slit, collimator, diffraction grating, focusing mirror, and detectors.[6]

However, the physical size and mass of optical components of a grating spectrometer, where the resolution is determined by the optical path difference, are still an issue for space applications. For example, four grating modules for SAFARI-SPICA with an R of 300 to cover a wavelength range between 34 and 230 μm have a maximal physical size varying from 0.4 to 0.5 meters.[4,6] The spectrometer becomes even more bulky and heavier when it aims to operate at longer wavelengths. In order to meet the requirements of forthcoming space observatories operating in FIR wavelengths, the development of a compact spectrometer with both high resolution and a wide bandwidth is imperative.

In the past decade, 2D planar metamaterials, known as metasurfaces, have attracted enormous amount of research interests.[7–20] Plentiful captivating metasurface devices have been designed, including vortex generators,[21,22] achromatic devices,[23–25] and multi-functional devices.[26–28] As a metasurface can encompass both dispersion and focusing functionalities within a single element, it holds promise as a viable replacement for conventional, bulky components such as gratings and focusing mirrors.

Several works on miniaturization of spectrometer structures by introducing a metasurface have been reported in the literature. However, most of them have been demonstrated at visible or other short wavelengths.[29] For example, Faraji-Dana et al.[30] proposed a concept of a compact spectrometer by folded metasurface optics made from a 1 mm thick glass slab with a volume of 7 mm³. The resolution R is 680 for the wavelengths from 760 to 860 nm. Nevertheless, the efficiency is 25% and is thus very low because of the multi-reflection between metasurfaces and dielectric loss. Thus, this architecture is not applicable to THz wavelengths. Zhu et al.[31] proposed a compact aberration-corrected spectrometer by a dispersive metasurface. The resolution R is 600 within a wavelength span between 450 and 700 nm. However, the efficiency is generally low because the focus point of the lens is off-axis. An alternative approach by Endo et al.[32] realizes a spectrometer on a chip, namely wide band radiation is spectrally separated by introducing superconducting filter banks. It was demonstrated at a longer wavelength of 860 μm. Such a

miniaturized spectrometer is limited to the working wavelengths that are roughly longer than 300 μm because of the use of available lossless superconductors. Until now, no practical compact spectrometers and in particular no metasurface based spectrometers have been reported at THz.

In this paper, we demonstrate a novel type of THz spectrometer, the core of which is a single metasurface consisting of 250 × 250 unit cells on a wafer. Each cell is a square of 45 × 45 μm², i.e., with the dimension being roughly a third of the wavelength. The schematic of our concept is illustrated in **Figure 1**. The THz wave in space is incident on the spectrometer (for simplicity, no telescope is included). The radiation of different wavelengths is deflected and focused on different positions in the focusing plane. We begin by modelling, then design and fabricate a metasurface sample, with the goal of optimizing its performance within a frequency span of 1.7 to 2.5 THz. Next, we use an array of quantum cascade lasers (QCLs) that operate at slightly different frequencies around 2.1 THz as input sources to validate our device performance by measuring resolution and efficiency of the spectrometer. Finally, we employ the spectral inversion algorithm to analyze experimental data and achieve a resolution R of 273. Our results demonstrate for the first time a compact and light weight THz metasurface spectrometer concept. This advance opens a new avenue for astronomic instruments for future space observatories.

2. Metasurface Spectrometer Concept

We propose the concept of a THz spectrometer in Figure 1b. The system includes one flat, reflective mirror and one metasurface that deflects and focuses the light. The incident light is a broadband, plane wave with an oblique angle θ_i of 30°. Incident light is reflected by the flat mirror onto the metasurface. Depending on the wavelengths, light is deflected and focused at different positions in the focusing plane. Here, we designed the metasurface working in reflection mode because in transmission, the efficiency is much lower than in reflection and the working bandwidth is also narrower.[33,34] The free and front views of a metasurface unit cell are shown in **Figure 2a,b**, respectively. The unit cell consists of three layers on a substrate: the bottom layer is
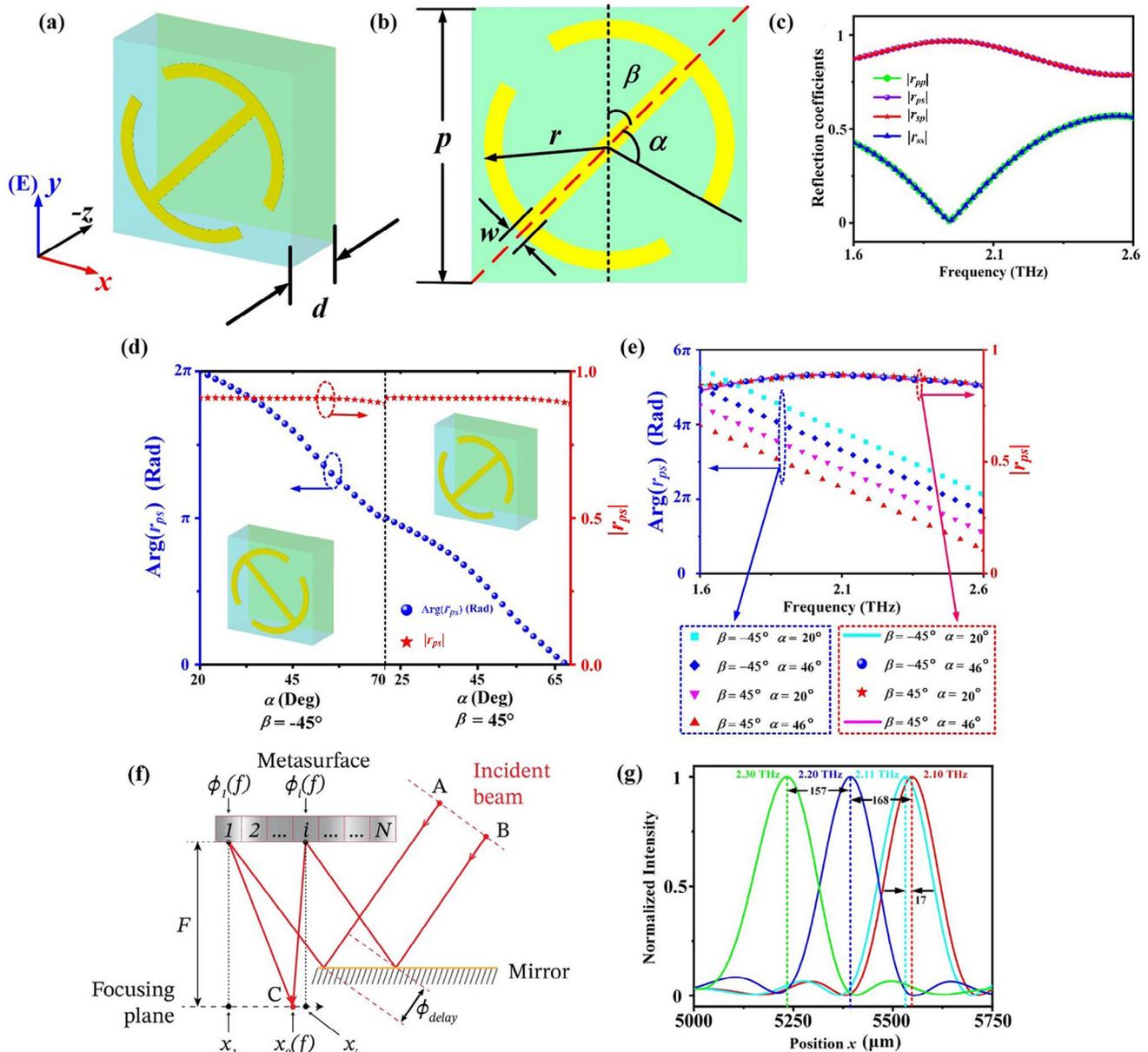
ADVANCED
SCIENCE NEWS
www.advancedsciencenews.com

LASER
& PHOTONICS
REVIEWS
www.lpr-journal.org

Figure 2. Metasurface spectrometer concept, design and simulation. a) Free view of a double-anchor unit cell for a metasurface. b) The front view of the double-anchor unit cell. c) The reflection properties of a unit cell for initial parameters as a function of the frequency. d) The phase and amplitude properties for different unit cell parameters at 2.1 THz. e) Broadband phase and amplitude response curves for parameters β switching from -45° to 45° α switching from 20° to 46°. f) Schematic of final design for metasurface spectrometer configuration. g) Intensity distribution that is normalized to its own maximal for different wavelengths in the focusing plane.

300 nm-thick gold (yellow color) with a conductivity of 3.3×10^7 S m^{-1}, which leads to a skin depth of less than 60 nm at 2 THz and ensures no transmission, but a high deflection efficiency for the THz waves. The middle layer is a dielectric made of polyimide (blue color) with a relative permittivity of 3.3 and loss tangent of $4 \times 10.^{-3}$[35] The top layer (on the polyamide) is also gold with a thickness of 100 nm and has the shape of double-anchor like structures (yellow color).[37,38]

To realize broadband and highly efficient deflection, we select the following initial values for the parameters for a double-

anchor as the unit cell. The dimension p of the unit cell is 45 μm, which also defines the periodicity of the metasurface. The parameters of the "shank" include a radius (r) of 21 μm, a width (w) of 3 μm, an angle (α) defining the length of the arm at 75°, and an angle (β) defining the orientation at 45°. The thickness d of the polyimide is 19 μm. The electromagnetic behavior of the double-anchor is characterized using CST Microwave Studio. In the simulation, the Frequency Domain Solver is used, and periodic boundary conditions are applied around the unit cell. The incident wave propagates with the oblique angle 30° relative to

ADVANCED
SCIENCE NEWS
www.advancedsciencenews.com

www.lpr-journal.org

LASER
& PHOTONICS
REVIEWS

z-axis. We use Reflection Jones Matrix[36] $J = \begin{bmatrix} r_{pp} & r_{ps} \\ r_{sp} & r_{ss} \end{bmatrix}$ to describe the reflection waves, where J is the reflection matrix, and r_{ij} represents the reflection coefficient of the i-polarized when the incidence is j-polarized wave with i and j being either p or s. We consider only the reflection here. The reflection properties of the double-anchor unit cell are shown in Figure 2c. If the unit cell is lossless, both $|r_{sp}|^2 + |r_{pp}|^2 = 1$ and $|r_{ps}|^2 + |r_{ss}|^2 = 1$ must be satisfied. We mainly concentrate on cross-polarization r_{ps}, the coefficient which is found to be above 0.8 across the whole frequency span. The phase of the reflection is determined by β and α. We give an example of the simulation results based on the unit cell working at 2.1 THz. In the left part of Figure 2d, if β is $-45°$ and α changes from 20° to 70°, we can realize the reflection phase coverage from 2π to π. In the right part, if β is 45° and α varies, the structure can realize the phase coverage from π to 0. In this way, the full 2π phase coverage is possible, which can be used to design the final metasurface. Furthermore, the reflection coefficient of such a unit cell is always above 90 % at 2.1 THz for different values of α and β.[37,38]

To study the bandwidth of the deflection response, we plot different phase and amplitude response curves in Figure 2e, where β switches between $-45°$ to 45° while α varies continuously. The structure can work well between 1.7 and 2.5 THz. All the phase curves are parallel, implying that within the entire band, the structures have a constant dispersion relationship.[23] In addition, within the band, all the reflection coefficients are always above 0.85, which ensures a high efficiency of the metasurface, which is generally defined as the ratio between the power of incoming beam and that of deflected one by the metasurface system.

Now, we introduce a spectrometer configuration based on the metasurface as shown in Figure 2f. The metasurface in the x direction consists of 250 double-anchor unit cells with varying α and β, which cover a length of 11.25 mm. In the y-direction, the same unit cells are repeated 250 times, leading to the same size as in the x-direction. Because of its invariance with respect to the y-coordinate, we call the configuration a 1D meta-surface structure. The focal length F of the metasurface is 15 mm for 2.1 THz. The distance between the metasurface and the flat mirror is 13 mm. We set the x-coordinate to zero in the left edge of the metasurface and set the y-coordinate equal to zero in the bottom edge of the metasurface. We obtain in the focusing plane a focused spot at position of 5.5 mm in the x-direction for 2.1 THz. The phase design of the unit cells in the metasurface is according to the constructive interference principle. As shown in Figure 2f, the optical path distance of ray A and B should be the same. The required phase response, which is the phase shift between the incident wave at a unit cell and the wave reflected by the unit cell, is determined for every unit cell by the following formula,[7]

$$\phi_i(f) = \phi_1(f)$$
$$+ \frac{2\pi f}{c}\left(\sqrt{[x_i - x_0(f)]^2 + F^2} - \sqrt{[x_1 - x_0(f)]^2 + F^2}\right) + \phi_{\text{delay}}$$

(1)

where, as seen in Figure 2f, $\phi_i(f)$ is the phase required for unit cell i at frequency f, $\phi_1(f)$ is the phase of the first unit cell at the left edge of the metasurface, $x_0(f)$ is the position of the focused beam in the focusing plane. c is the speed of light, x_i is the center of unit cell i, and ϕ_{delay} is the phase due to the additional path as shown in the figure. Because of the plane wave assumption, the equal phase plane is perpendicular to the propagation direction of the incident wave, thus, $\phi_{\text{delay}} = x_i \sin\theta_i \frac{2\pi f}{c}$. To satisfy the required phase in Equation (1), we select the proper α and β for all double-anchors of all cells of the metasurface. The values of parameters α and β for every unit cell can be found in Section S1 (Supporting Information).

Next, we perform simulations for the spectrometer configuration using CST Microwave studio, where the Time-Domain Solver is again applied. The incident field light is a broadband plane wave, with the electric field in y-direction, and covers the full area of the metasurface. We calculate the intensity distribution of p-polarized field for a few different wavelengths in the focusing plane. The results are plotted in Figure 2g. The peak position of deflected beam for 2.10 THz, 2.11 THz, 2.20 THz, and 2.30 THz is at 5552, 5535, 5384, and 5227 μm in x-axis, respectively. Simulated half power beam width for 2.10, 2.11, 2.20, and 2.30 THz is 162, 164 177, and 190 μm, respectively. Furthermore, peak positions within 0.01 THz at 2.1 THz are distinguishable, thus the spectral resolution R is at least 210. We also normalized all of curves again with respect to the peak of 2.10 THz curve in Figure S1a of Section S2 (Supporting Information). In addition, we calculate and give the intensity distribution from 1.7 to 2.5 THz with 0.10 THz spacing normalized with the peak of 2.10 THz curve in Figure S1b (Supporting Information) and the efficiency for each frequency in Table S1 (Supporting Information). The result suggests the maximal efficiency of 80.4 % at 2.1 THz and an effective bandwidth of 30 % using a 3 dB criteria. The results are discussed in Section S2 (Supporting Information). This bandwidth is comparable with ≈50% of grating spectrometers required in refs. [4–6].

We also calculated the intensity distribution of the s-component of the reflection wave in the focusing plane (again, for the s-polarized incident wave) from the metasurface. The results are discussed in Section S3 (Supporting Information).

3. Fabrication and Experimental Set-Up

The fabrication of the metasurface consists of three key steps. Firstly, an Au layer of 300 nm is deposited on a silicon wafer. Then, a polyimide layer of 19 μm thick is spin-coated on top of the Au layer. A second Au layer of 100 nm thick is deposited atop the polyimide and is subsequently patterned by photolithography and etching to form periodic double-anchor structures. The schematic of the cross section of a completed metasurface sample and an optical micrograph of its surface are shown in **Figure 3a**. The other part of the wafer, without the second Au layer, but with the polyimide layer and the first Au layer, will serve for flat mirrors described in this work.

We have built an experimental setup shown in Figure 3b to characterize the spectrometer, where the metasurface structure on a holder, together with a flat mirror on another wafer, is shown in Figure 3c. Both the metasurface and mirror have a maximum
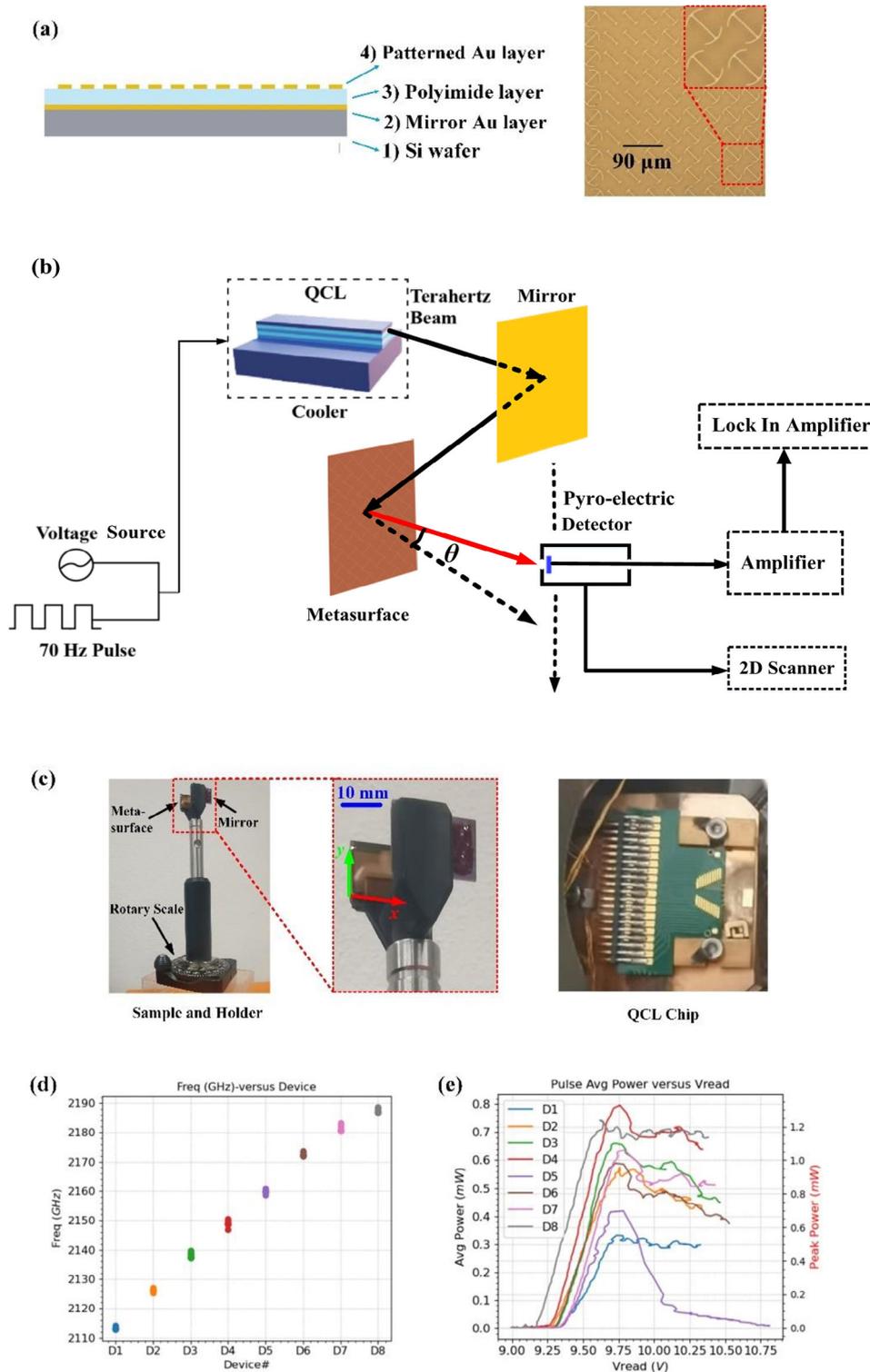
ADVANCED
SCIENCE NEWS

www.advancedsciencenews.com

LASER
& PHOTONICS
REVIEWS

www.lpr-journal.org

Figure 3. Metasurface structure and experimental set-up. a) Schematic cross-section of the metasurface structure and fabricated sample. b) Schematic overview of the entire experimental setup for characterizing a metasurface spectrometer system. c) Pictures of a metasurface sample and a flat mirror on a holder and the chip containing the QCLs. d) The frequencies for the 8 QCLs. e) Average power curves against voltage source for 8 different QCLs on the chip.

size of 15 mm, making them very compact. Their weights are negligibly low due to the Si wafers. Before we explain how the experiment was done, we first mention the THz quantum cascaded lasers (QCLs) as calibration sources. The distributed feedback (DFB) laser array (SN556) contains 8 individual lasers on one chip (see Figure 3c) with nominal peak power of 1 mW at a working temperature of 49 K (see Figure 3e), emitting the radiation in the range of 2.11 to 2.19 THz as shown in Figure 3d. The gain medium used for the QCLs is based on resonant phonon (RP) depopulation[39] scheme with a two-level injector. The frequency selectivity of the lasers is provided by DFB structure based on the antenna-coupled wire laser design as demonstrated in.[40,41] All lasers in the array maintain single-mode operation. The advantages associated with QCLs encompass features such as coherent emission characterized by an exceptionally narrow linewidth, typically less than 1 MHz,[42] as well a robust output power profile. The high output power capability of QCLs facilitates the utilization of a room temperature detector, significantly simplifying the experimental setup.

To obtain the position of a deflected/focused beam in the focusing plane, we use a pyro-electric detector (in Figure 3b) with a NEP (Noise-equivalent power) of 5×10^{-9} W Hz$^{-1/2}$ and with a pinhole of 100 μm in diameter in front of the detector. The detector, mounted on a computer controlled 2D translation stage, is used to map the intensity of deflected beam by raster scanning in a step of 100 μm along the focusing plane. However, when we do only 1D fine scanning, we reduce the pinhole to 30 μm, while we scan in a reduced step of 10 μm. We make use of only three QCLs in our experiment: D4 at 2.150 THz, D7 at 2.180 THz, and D8 at 2.188 THz, where the frequencies were determined separately by an FTS. The frequency difference between D7 and D8 is of interest because it is only 8 GHz, which is the smallest in the chip. We target to distinguish them (D7 and D8 lines) to demonstrate a high spectral resolution. Furthermore, these three lasers have higher output power than the rest. We operate the QCLs in a Stirling cooler. More information about the QCLs is given in Figure S3 of Section S4 (Supporting Information).

4. Experimental Results and Data Analysis with Spectrum Inversion Method

QCL beams deviate considerably from a Gaussian beam partly due to the QCL itself and partly due to non-optimized optics inside the cooler. To determine the peak position of the deflected beam accurately, we use a diaphragm with a variable aperture from 4 to 2.5 mm in diameter to filter the beam to a circular, symmetric beam. The method is described in Section S5 (Supporting Information). We also note that a change of incident beam size does not influence the position of the focus and the deflection effect of the metasurface but can affect the focused spot size because of the change of the numerical aperture (NA). The simulated intensity distribution in focusing plane for different beam size of the incidence at 2.10 THz is discussed in Section S6 (Supporting Information).

We begin with a measurement of the metasurface at 2.150 THz using QCL D4. We first characterize the THz beam using another flat mirror instead of the metasurface, with the same dimension and at the same position. The schematic of measurement configuration is illustrated in **Figure 4a**. The beam is measured at the

focusing plane as shown in Figure 4b. The measured beam in this case is 4 mm in diameter. Due to replacement of the metasurface by the flat mirror, the measured beam reveals the properties of the incident beam while the beam position is purely due to the dispersion-less reflection, i.e., there is no focusing effect. Then, we replace the flat mirror with the metasurface as shown in Figure 4c and repeat the measurement. The measured beam at the focusing plane, which is shown in Figure 4d, shows that the deflected beam shifts to the right with a distance of 7.6 mm with respect to the (directly) reflected beam and the beam becomes much narrower in the x-direction. In the same plot, the direct reflection is visible but has a much lower intensity. Apparently, we have observed a signature of the 1D metasurface, which deflects and focuses the beam at only horizonal direction. To quantify the deflected beam and compare it with the simulations, we make 1D measurements of the two cases by fine scanning the detector in the x-direction along the center of the beam, as indicated by the yellow dotted line. The results are summarized in Figure 4e. The beam (center) shifts from -3.31 to 5.09 mm. The half power beam widths of reflected beam and deflected beam (in the x-direction) are 4.03 and 0.37 mm, respectively. The relative shift in distance will be compared to the simulation later. We now compare the measured deflected beam profile with our modeling in Figure 4f, where we found that the measured beam has a similar profile as the one from the simulation, except the width is 70% wider. This difference is mainly due to the narrower incident beam (of 4 mm) in the experiment than full illumination to the metasurface as assumed in the simulation, which leads to a smaller NA and hence not perfectly focused on the focusing plane. We also estimate the experimental efficiency of the metasurface, which is defined as the ratio between the power of deflected beam by the metasurface and one mirror and that of incoming beam after two reflection mirrors. The relative power of the incident beam is determined by integrating the total intensity within the beam area, while the power of the deflected beam is estimated by integrating the intensity of the beam in Figure 4d. The efficiency, thus the ratio between the two, is 78.4%, which is close to the simulated one (80.4 % at 2.1 THz). The loss comes mainly from the direct reflection, which is known to be 12.7%, and from the resonant loss from double-anchor gold structures and random wave scattering, which are assumed to be 8.9%.

We repeat the measurements at 2.180 THz using QCL D7, but with its output beam filtered by a smaller aperture of 3 mm. **Figure 5a** shows measured reflected beam using the mirror, while Figure 5b plots the beam deflected by the metasurface. As expected, the deflected beam is shifted with respect to the reflected one and is also focused. We measure the 1D intensity distribution of the beams along the yellow dot lines in Figure 5a,b, which are plotted together in Figure 5c for a comparison. The beam shifts from the position of $x = -3.29$ mm to x = 5.03 mm. The half power beam widths of reflected beam and deflected beam are 3.04 mm and 0.45 mm, respectively. We also plot deflected/focused beam in detail to allow for a comparison between measurement and simulation in Figure 5d. We continue to characterize the metasurface at 2.188 THz, using the third laser QCL D8, applying an even smaller aperture of 2.5 mm to filter the beam because otherwise the beam is not circular enough. All the results, similar to the other two frequencies, are summarized in Figure 5e–h. The beam shifts from -3.33 mm to 5.01 mm. The
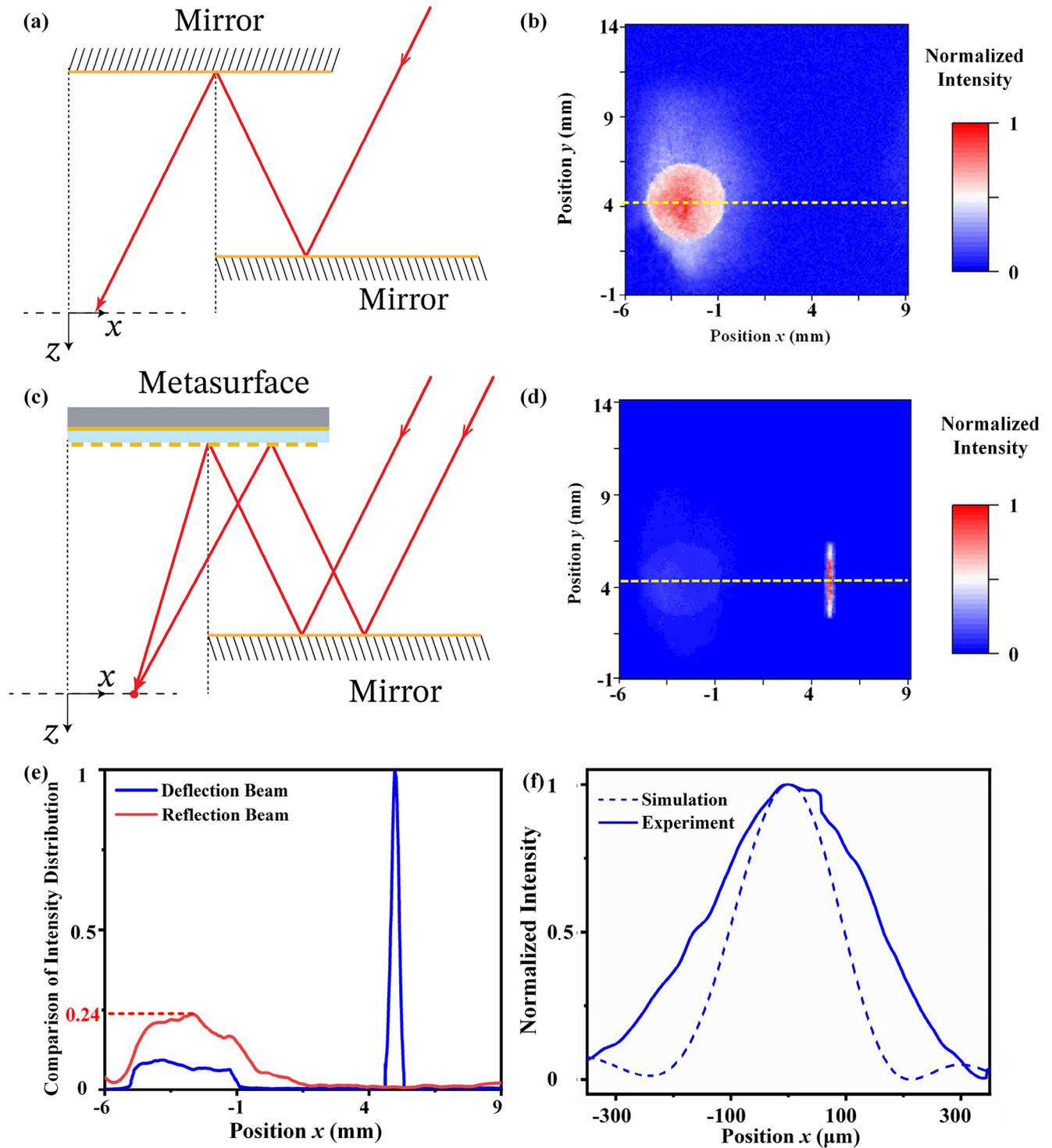
Figure 4. Measurement results of the metasurface spectrometer structure at 2.15 THz. a) Schematic of the setup when the metasurface is replaced by a mirror. b) Measured reflection beam using the setup in (a). c) Schematic of the metasurface spectrometer set up. d) Measured deflection beam focused intensity using the setup in (c). e) Measured cross-section of the intensity distributions of the reflected and deflected beam along the dashed lines indicated in (b,d). f) Comparison of the measured and simulated intensity distributions of the deflected beams.
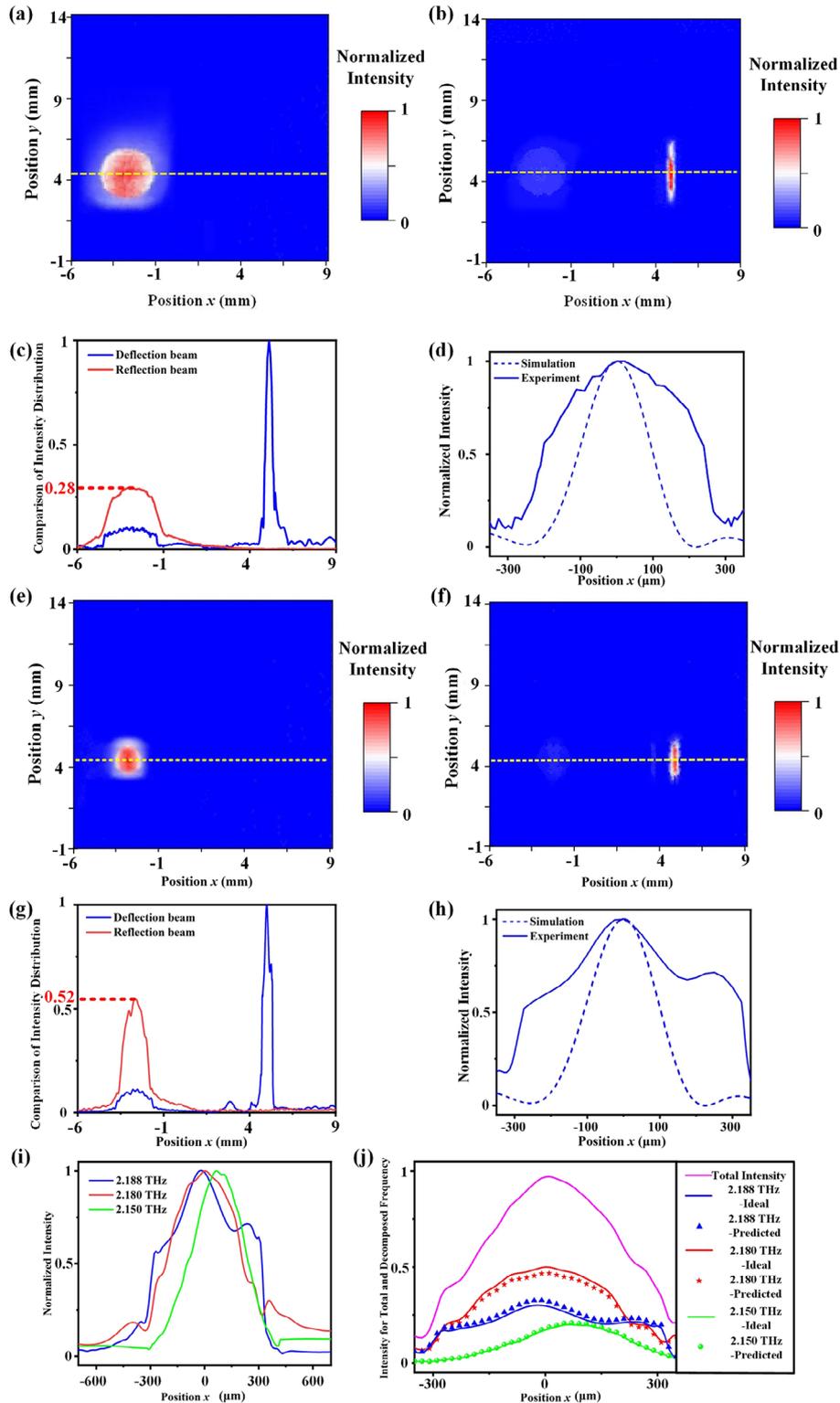
Figure 5. Measurement results of the metasurface spectrometer structure at 2.180 and 2.188 THz. a) Reflected beam b) deflected beam at 2.180 THz. c) Cross-section of the intensity distributions of the reflected and deflected beam along the dashed lines in (a,b). d) Comparison of the measured and simulated intensity distributions of the deflected beam for 2.180 THz. e) Reflected beam at 2.188 THz. f) Deflected beam. g) Cross-section of the intensity distributions of the reflected and deflected beam along the dashed lines in (e,f). h) Comparison of measured and simulated intensity distributions of the deflected beam at 2.188 THz. i) Intensity distributions of the deflected beams for the three frequencies. j) The total intensity distribution obtained by summing the intensity distributions for 2.150, 2.180, 2.188 THz from (i), weighted by factors 0.2, 0.5, and 0.3, respectively. Also plotted are the three intensity distributions derived by the spectrum inversion method together with the weighted intensity distributions used in (j).

Table 1. Comparison of the metasurface spectrometer and grating spectrometers at FIR, excluding the detectors. The key performance metrics include spectral-resolution, efficiency of the grating or metasurface (referred to the definition in the texts), working bandwidth, and dimensions.

Type	Spectral-resolution ($\lambda/\Delta\lambda$)	Efficiency	Bandwidth	Dimension
Grating spectrometers[4]	300	≥65%[48]	50 %	Max size = 400–500 mm, including a grating and a focusing mirror
Metasurface spectrometer	60[a] –270[b]	78%	30 % (at 2.1 THz)	Max size = 15 mm (11 mm × 9 mm × 15 mm)

[a] Observed directly; [b] Applying the Spectrum inversion method.

half power beam width of reflected beam and deflected beam are 2.69 and 0.59 mm, respectively. We notice two anomalies here: One is the unexpected weak peak at the position of 2.9 mm in Figure 5g, the reason for which is unclear, and other is the beam width in Figure 5h, which is considerably larger than the modeling due to the smaller input beam size.

We plot deflected beams at the three frequencies together in Figure 5i to quantify the frequency dependence. The peak position of the beam profile for 2.180 THz is defined to be at $x = 0$. Then, the relative peak position for 2.150 THz is 60 µm in experiment, while 45 µm predicted in simulation. The peak position of 2.188 THz is at x = −20 µm in experiment, while −17 µm in simulation. With respect to the peak positions, experimental values agree reasonably well with the simulations. Furthermore, since we can observe the position difference when two lights around 2.188 THz with only a difference of 8 GHz, we seem to achieve a spectral resolution R of 273. However, suppose these three coherent signals are simultaneously shined onto the metasurface structure, it should be possible to distinguish the 2.150 and 2.188 THz lines, resulting in an R of 58. However, it may be difficult to discriminate between the closely spaced 2.150 THz and 2.180 THz lines, as suggested by Figure 5i. In this case we can introduce the spectrum inversion algorithm to resolve these lines. The details of the spectrum inversion algorithm are described in Section S7 (Supporting Information). To apply this method to our experimental data, we sum three intensity profiles using the weights of 0.2, 0.5, and 0.3 for the measured profile at 2.150 THz, 2.180 THz, 2.188 THz in Figure 5i. It leads to summed intensity profile contributed by three different frequencies in Figure 5j. We furthermore assume a realistic signal-to-noise (S/N) ratio of 30 dB for our measurements. By applying the spectrum inversion technique, we find that the power weight to be 0.209 for 2.150 THz, which differs by 4.5% from the original 0.2. Furthermore, the power weight obtained for 2.180 THz is 0.468 with an error of 6.4% and is 0.326 for 2.188 THz with an error of 8.7%. Thus, the max uncertainty is 8.7% which is still reasonably small. The comparison of ideal and predicted intensity distributions for each frequency is also shown in Figure 5j. Because we are able to differentiate two lines separated by 8 GHz at 2.19 THz, we have realized a resolution R of at least 273.

We compare the key performance metrics of our metasurface spectrometer with those of FIR grating spectrometers in[6,48] in terms of spectral resolution, efficiency, bandwidth, and relevant dimensions, as shown in **Table 1**. While the overall performance of the metasurface spectrometer is slightly worse than that of grating spectrometers, it remains comparable. However, the metasurface spectrometer is significantly more compact and

clearly has a lower weight, although the latter is not included in the table.

5. Conclusion and Outlook

In summary, we propose and demonstrate a centimeter-sized THz spectrometer based on a metasurface, which functions both in deflection and focusing. We designed, modeled, and fabricated a metasurface to work in the frequency centered at 2.1 THz with a bandwidth of 30%. We have used three quantum cascaded lasers, emitting slightly different frequencies around 2.1 THz, to verify our concept, particularly the spectral resolution. The deflected beams can show different positions in the focusing plane for different frequencies and the different positions are sufficient even for two laser lines with only 8 GHz difference. This result implies a spectral resolution R of 273. However, to fully resolve them, we apply the spectral inversion method by making use of the known frequency information. The efficiency of the metasurface in the spectrometer was found to be 78.4 % at 2.15 THz. The results suggest that we succeeded for the first time in demonstrating a compact spectrometer using a metasurface at THz, which can be adjusted to other THz frequencies. To cover a wider frequency range, one can use several metasurface spectrometers, being similar to the grating spectrometers using a couple of grating modules.[4–6] Such a centimeter-sized and low weight spectrometer has potential to replace classic, half meter sized bulky and heavy grating spectrometers available for space observatories[4–6] and the same concept can be applied to other wavelengths., e.g., medium- IR (5–30 µm) grating spectrometer for the JWST-MIRI instrument.[43] Of course, it offers a solution to realize handheld, portable spectrometers at THz wavelengths for the earth observations and even various non-space applications.

To further increase the spectral resolution, one needs to optimize the design of the metasurface to enhance the dispersion and to increase NA properly. Another modification is to explore a 2D metasurface to improve the intensity in the center of focus beam because the 2D metasurface has the effect of 2D focus, which increases the S/N ratio. Finally, the spectrometer system should be integrated with ultra-sensitive cryogenic detector arrays[44–46] for space observatories, while with a suitable room temperature 2D detector arrays[47] for non-space applications.

Supporting Information

Supporting Information is available from the Wiley Online Library or from the author.

2401290 (9 of 11)

© 2024 The Author(s). Laser & Photonics Reviews published by Wiley-VCH GmbH

Conflict of Interest

Tsung-Yu Kao and Alan Lee work in LongWave Photonics LLC, USA.

Data Availability Statement

The data that support the findings of this study are available from the corresponding author upon reasonable request.

[1] D. Farrah, K. E. Smith, D. Ardila, C. M. Bradford, M. Dipirro, C. Ferkinhoff, J. Glenn, P. Goldsmith, D. Leisawitz, T. Nikola, N. Rangwala, S. A. Rinehart, J. Staguhn, M. Zemcov, J. Zmuidzinas, J. Bartlett, *J. Astron. Telesc., Instrum., Syst.* **2019**, *5*, 020901.

[2] A. Leitenstorfer, A. S. Moskalenko, T. Kampfrath, J. Kono, E. Castro-Camus, K. Peng, N. Qureshi, D. Turchinovich, K. Tanaka, A. G. Markelz, M. Havenith, C. Hough, H. J. Joyce, W. J. Padilla, B. Zhou, K.-Y. Kim, X.-C. Zhang, P. U. Jepsen, S. Dhillon, M. Vitiello, E. Linfield, A. G. Davies, M. C. Hoffmann, R. Lewis, M. Tonouchi, P. Klarskov, T. S. Seifert, Y. A. Gerasimenko, D. Mihailovic, R. Huber, et al., *J. Phys. D: Appl. Phys.* **2023**, *56*, 223001.

[3] G. L. Pilbratt, J. R. Riedinger, T. Passvogel, G. Crone, D. Doyle, U. Gageur, A. M. Heras, C. Jewell, L. Metcalfe, S. Ott, M. Schmidt, *Astron. Astrophys.* **2010**, *518*, L1.

[4] P. R. Roelfsema, H. Shibai, L. Armus, D. Arrazola, M. Audard, M. D. Bradford, I. Charles, P. Dieleman, Y. Doi, L. Duband, M. Eggens, J. Evers, I. Funaki, J. R. Gao, M. Giard, A. di Giorgio, L. M. G. Fernández, M. Griffin, F. P. Helmich, R. Hijmering, R. Huisman, D. Ishihara, N. Isobe, B. Jackson, H. Jacobs, W. Jellema, I. Kamp, H. Kaneda, M. Kawada, F. Kemper, et al., *I. Publ. Astron. Soc. Aust.* **2018**, *35*, e030.

[5] C. M. Bradford, B. Cameron, B. Moore, S. Hailey-Dunsheath, E. Amatucci, D. Bradley, J. Corsetti, D. Leisawitz, M. DiPirro, J. Tuttle, A. Brown, D. McBirney, A. Pope, L. Armus, M. Meixner, K. Pontoppidan, *J. Astron. Telesc., Instrum., Syst.* **2021**, *7*, 011017.

[6] J. Glenn, C. M. Bradford, E. Rosolowsky, R. Amini, K. Alatalo, L. Armus, A. J. Benson, T.-C. Chang, J. Darling, P. K. Day, J. Domber, D. Farrah, B. Hensley, S. Lipscy, B. Moore, S. Oliver, J. Perido, D. Redding, M. Rodgers, R. Shirley, H. A. Smith, J. B. Steeves, C. Tucker, J. Zmuidzinas, *J. Astron. Telesc., Instrum., Syst.* **2021**, *7*, 034004.

[7] N. Yu, P. Genevet, M. A. Kats, F. Aieta, J. P. Tetienne, F. Capasso, Z. Gaburro, *Science* **2011**, *334*, 333.

[8] A. Arbabi, Y. Horie, M. Bagheri, A. Faraon, *Nat. Nanotechnol.* **2015**, *10*, 937.

[9] N. Yu, F. Capasso, *Nat. Mater.* **2014**, *13*, 139.

[10] S. Zhang, *Light: Sci. Appl.* **2020**, *9*, 94.

[11] A. S. Solntsev, G. S. Agarwal, Y. S. Kivshar, *Nat. Photonics* **2021**, *15*, 327.

[12] T. Gu, H. J. Kim, C. Rivero-Baleine, J. Hu, *Nat. Photonics* **2023**, *17*, 48.

[13] D. N. Neshev, A. E. Miroshnichenko, *Nat. Photonics* **2023**, *17*, 26.

[14] J. C. Ndukaife, *Nat. Nanotechnol.* **2022**, *17*, 1042.

[15] H. Ren, X. Fang, J. Jang, J. Bürger, J. Rho, S. A. Maier, *Nat. Nanotechnol.* **2020**, *15*, 948.

[16] S. Lepeshov, A. Krasnok, *Nat. Nanotechnol.* **2021**, *16*, 615.

[17] A. M. Shaltout, V. M. Shalaev, M. L. Brongersma, *Science* **2019**, *364*, eaat3100.

[18] Q. Song, M. Odeh, J. Zúñiga-Pérez, B. Kanté, P. Genevet, *Science* **2021**, *373*, 1133.

[19] A. L. Holsteen, A. F. Cihan, M. L. Brongersma, *Science* **2019**, *365*, 257.

[20] W. Ji, J. Chang, H. X. Xu, J. R. Gao, S. Gröblacher, H. P. Urbach, A. J. Adam, *Light: Sci. Appl.* **2023**, *12*, 169.

[21] K. Zhang, Y. Wang, Y. Yuan, S. N. Burokur, *Appl. Sci.* **2020**, *10*, 1015.

[22] Y. Bao, J. Ni, C. W. Qiu, *Adv. Mater.* **2020**, *32*, 1905659.

[23] W. Ji, T. Cai, Z. Xi, P. Urbach, *Laser Photonics Rev.* **2022**, *16*, 2100333.

[24] A. Ndao, L. Hsu, J. Ha, J. H. Park, C. Chang-Hasnain, B. Kanté, *Nat. Commun.* **2020**, *11*, 3205.

[25] F. Balli, M. Sultan, S. K. Lami, J. T. Hastings, *Nat. Commun.* **2020**, *11*, 3892.

[26] S. Chen, W. Liu, Z. Li, H. Cheng, J. Tian, *Adv. Mater.* **2020**, *32*, 1805912.

[27] W. Ma, Y. Xu, B. Xiong, L. Deng, R. W. Peng, M. Wang, Y. Liu, *Adv. Mater.* **2022**, *34*, 2110022.

[28] S. Grabarnik, A. Emadi, H. Wu, G. De Graaf, R. F. Wolffenbuttel, *Appl. Opt.* **2008**, *47*, 6442.

[29] Z. Yang, T. Albrow-Owen, W. Cai, T. Hasan, *Science* **2021**, *371*, eabe0722.

[30] M. Faraji-Dana, E. Arbabi, A. Arbabi, S. M. Kamali, H. Kwon, A. Faraon, *Nat. Commun.* **2018**, *9*, 4196.

[31] A. Y. Zhu, W. T. Chen, J. Sisler, K. M. Yousef, E. Lee, Y. W. Huang, C. W. Qiu, F. Capasso, *Adv. Opt. Mater.* **2019**, *7*, 1801144.

[32] A. Endo, K. Karatsu, A. P. Laguna, B. Mirzaei, R. Huiting, D. J. Thoen, V. Murugesan, S. J. C. Yates, J. Bueno, N. V. Marrewijk, S. Bosma, O. Yurduseven, N. Llombart, J. Suzuki, M. Naruse, P. J. d. Visser, P. v. d. Werf, T. M. Klapwijk, J. J. Baselmans, *J. Astron. Telesc., Instrum., Syst.* **2019**, *5*, 035004.

[33] G. Zheng, H. Mühlenbernd, M. Kenney, G. Li, T. Zentgraf, S. Zhang, *Nat. Nanotechnol.* **2015**, *10*, 308.

[34] A. Arbabi, E. Arbabi, Y. Horie, S. M. Kamali, A. Faraon, *Nat. Photonics* **2017**, *11*, 415.

[35] S. Sahin, N. K. Nahar, K. Sertel, *J. Infrared, Millimeter, Terahertz Waves* **2019**, *40*, 557.

[36] Y. Bao, L. Wen, Q. Chen, C. W. Qiu, B. Li, *Sci. Adv.* **2021**, *7*, eabh0365.

[37] H. P. Li, G. M. Wang, T. Cai, J. G. Liang, X. J. Gao, *IEEE Trans. Antennas Propag.* **2018**, *66*, 5121.

[38] H. X. Xu, G. Hu, Y. Wang, C. Wang, M. Wang, S. Wang, Y. Huang, P. Genevet, W. Huang, C. W. Qiu, *Light: Sci. Appl.* **2021**, *10*, 75.

[39] Q. Hu, B. S. Williams, S. Kumar, H. Callebaut, S. Kohen, J. L. Reno, *Semicond. Sci. Technol.* **2005**, *20*, S228.

[40] T. Y. Kao, X. Cai, A. W. Lee, J. L. Reno, Q. Hu, *Opt. Express* **2015**, *23*, 17091.

[41] T. Y. Kao, Q. Hu, J. L. Reno, *Opt. Lett.* **2012**, *37*, 2070.

[42] Y. Ren, J. N. Hovenier, M. Cui, D. J. Hayton, J. R. Gao, T. M. Klapwijk, S. C. Shi, T.-Y. Kao, Q. Hu, J. L. Reno, *Appl. Phys. Lett.* **2012**, *100*, 041111.

[43] M. Wells, J.-W. Pel, A. Glasse, G. S. Wright, G. Aitink-Kroes, R. Azzollini, S. Beard, B. R. Brandl, A. Gallie, V. C. Geers, A. M. Glauser, P. Hastings, T. Henning, R. Jager, K. Justtanont, B. Kruizinga, F. Lahuis, D. Lee, I. Martinez-Delgado, J. R. Martínez-Galarza, M. Meijers, J. E. Morrison, F. Müller, T. Nakos,

B. O'Sullivan, A. Oudenhuysen, P. Parr-Burman, E. Pauwels, R.-R. Rohloff, E. Schmalzl, et al., *Publ. Astron. Soc. Pac.* **2015**, *127*, 646.

[44] P. M. Echternach, B. J. Pepper, T. Reck, C. M. Bradford, *Nat. Astron.* **2018**, *2*, 90.

[45] J. J. A. Baselmans, J. Bueno, S. J. C. Yates, O. Yurduseven, N. Llombart, K. Karatsu, A. M. Baryshev, L. Ferrari, A. Endo, D. J. Thoen, P. J. de Visser, R. M. J. Janssen, V. Murugesan, E. F. C. Driessen, G. Coiffard, J. martin-Pintado, P. Hargrave, M. Griffin, *Astron. Astrophys.* **2017**, *601*, A89.

[46] M. D. Audley, G. de Lange, J.- R. Gao, P. Khosropanah, R. Hijmering, M. Ridder, P. D. Mauskopf, D. Morozov, N. A. Trappe, S. Doherty, *Rev. Sci. Instrum.* **2016**, *87*, 043103.

[47] S. Boppel, A. Lisauskas, M. Mundt, D. Seliuta, L. Minkevicius, I. Kasalynas, G. Valusis, M. Mittendorff, S. Winnerl, V. Krozer, H. G. Roskos, *IEEE Trans. Microwave Theory Tech.* **2012**, *60*, 3834.

[48] A. Cuadrado, M. Fernández-Rodríguez, L. M. Sanchez-Brea, G. García-Lozano, G. Mercant, M. C. Torquemada, J. Alda, L. M. González, T. Belenguer, *IEEE Trans. Terahertz Sci. Technol.* **2023**, *13*, 605.